Biotechnology for Biofuels and Bioproducts

RESEARCH

Open Access

Fine-tuning xylan side chains for enhanced production of high-yield sugars, fine-shaped nanocrystals, and stable Pickering emulsions in *Arabidopsis thaliana*

Sufang Li[1,2,3], Min Li[1], Hailang Wang[2,3], Tianqi Li[3], Zhen Hu[1], Yanting Wang[2], Peng Chen[3], Zhaosheng Kong[1], Liangcai Peng[2,3] and Youmei Wang[1*]

Abstract

Arabinoxylans are complex polysaccharides found in the secondary cell walls of plants, and their substitution patterns of arabinose (Ara) and glucuronic acid (GlcA) significantly affect their properties for structural and bio-functional applications. In this study, we engineered xylan side chains by overexpressing the arabinosyltransferase *AtXAT2* in both wild-type *Arabidopsis* and a glucuronic acid-deficient mutant (*atdgux*). The genetically modified xylan substrates were subsequently utilized to prepare nanocrystals and Pickering emulsions. Notably, nanocrystals derived from lower-substituted xylan displayed more ordered arrangements and higher crystallinity, while conventional xylan substrates exhibited superior emulsifying properties. Furthermore, the modification of xylan side chains significantly influenced the alignment and crystallinity of cellulose microfibrils, enhancing biomass saccharification and reducing cellulose nanocrystal dimensions. This study thus illustrates an effective strategy for achieving diverse and valuable bioproduction through precise genetic engineering of xylan in plants and provides valuable insights into the dynamic mediation of xylan and the construction of cell wall networks.

Keywords AtXAT2, Xylan structure engineering, Pickering emulsion, Biomass saccharification, Cellulose nanocrystals

*Correspondence:
Youmei Wang
wym@sxau.edu.cn
Full list of author information is available at the end of the article

Graphical Abstract

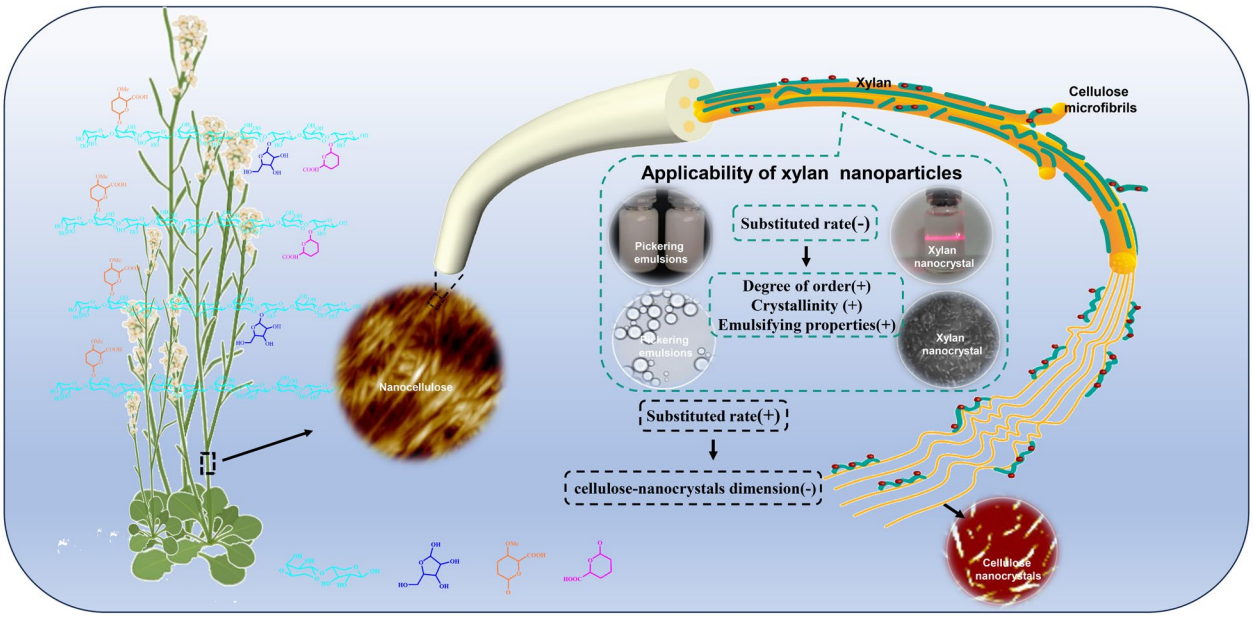

Introduction

Xylan, one of the most abundant hemicelluloses in the secondary cell walls of vascular plants, is characterized by its abundance, renewability, and biodegradability [1]. Its unique chemical modifiability and cost-effectiveness have made it an ideal precursor for the development of advanced functional materials, offering significant advantages in this area [2, 3]. Through molecular structure design and chemical modification, a variety of high-performance material systems have been successfully developed based on xylan [4, 5], including nanoparticles [6–10], flexible films [11, 12], emulsifiers [13], and multifunctional hydrogels [14]. However, in relation to the plant cell wall itself, xylan acts as a "molecular adhesive", forming both covalent and non-covalent cross-links with lignin and cellulose microfibrils to maintain the stability of the cell wall network structure [15–19]. The structure of xylan significantly influences the network structure of the cell wall, the extractability of lignin–carbohydrate complexes, and the ultrastructure of cellulose fibrils [13, 20], while also affecting the extraction and separation of cell wall polymers and the performance of bioproducts [21–23]. However, research on how the molecular structure of xylan influences the performance of bio-functional materials remains limited. This gap in fundamental theoretical understanding represents a significant barrier to the rational design and functional optimization of high-performance hemicellulose-based composites.

Xylan consists of a linear chain of β−1,4-linked xylosyl residues as backbone, along with various side-chain substitutions, including α−1,2- or α−1,3-linked arabinofuranose (Ara*f*), (4-O-methyl) glucuronic acid (GlcA/MeGlcA), and numerous acetylation modifications [24–27]. The side-chain modifications of xylan are of paramount importance for its utilization in various biological and industrial applications [28, 29]. During the industrial extraction process, most of the xylan branches are typically removed, resulting in a linear structure primarily composed of xylose units [30, 31]. This low-branched linear configuration makes xylan highly susceptible to forming crystalline structures, which has significant implications for its subsequent processing and utilization [32, 33]. Our previous research has also shown that the degree of arabinose substitution on xylan directly affects the morphology of nanoparticles and their potential applications in novel materials [34]. This strongly suggests that different side-chain modifications impart xylan with varied application potentials and functional properties.

Based on the source of the raw material, xylan can be classified into three main types: arabinoxylan (AX), glucuronoxylan (GX), and glucuronoarabinoxylan (GAX) [35]. In the model dicot *Arabidopsis thaliana*, xylan is

characterized as GAX, which is sparsely arabinosylated and predominantly features GlcA and MeGlcA appendages [36]. Five members of the GT8 subfamily within the Carbohydrate-Active Enzymes (CAZy) family, namely GUX1 to GUX5, have been identified as key enzymes in the process of xylan glucuronidation [36–38]. In the loss-of-function mutants of GUX1 and GUX2, GlcA side chains are nearly undetectable, highlighting their essential roles in this modification process [39, 40]. Due to the absence of Ara side chains in the xylan of *Arabidopsis*, the double gene knockout mutants of GUX1 and GUX2 also lack GlcA modifications. This unique genetic background makes them ideal transformation vectors commonly used to study the functions of related glycosyltransferases [38, 39, 41]. At the same time, it also provides a reliable material model for investigating the effects of xylan side-chain modifications on the properties of biomass-derived functional materials.

Multiple glycosyltransferases belonging to the GT61 family have been identified as key players in the arabinofuranose (Ara*f*) substitution of grass xylan [42, 43]. The GT61 glycosyltransferase family comprises three conserved clades (A, B, C). Clade A underwent grass-specific expansion, yielding 19 members in rice compared to 2 in *Arabidopsis* [44, 45]. This genomic disparity reflects the abundance of Ara decorations on grass xylans, which are nearly absent in the dicot lineage. Research in wheat has revealed that the TaXAT1 and TaXAT2 from clade A of the GT61 family are involved in the addition of Ara side chains to xylan, which is consistent with reports of the catalytic arabinosylation activity of OsXAT2/OsXAT3/OsXAT4/OsXAT5/OsXAT6 in rice [43, 44]. When these enzymes were expressed heterologously in the *atdgux* mutant of *Arabidopsis*, the addition of Ara modifications to xylan side chains was detected, providing strong evidence for their unique activities and suggesting that the branching of Ara on *Arabidopsis* xylan can be achieved through the expression of arabinosyltransferase [46, 47]. Overall, the enzyme activity of the GT61 family A branch is highly conserved in monocots, including rice OsXAT2/3/4/5/6 and wheat TaXAT1/2, forming the core enzymatic machinery responsible for installing Ara modifications on xylan [25, 44]. Furthermore, biochemical assays indicate that the core protein OsXAT2 in rice is a strict 3-O-arabinosyltransferase, specifically transferring Ara*f* to the 3-O position of xylosyl residues within the xylan backbone [43]. Although the homologous gene *AtXAT2* in *Arabidopsis* is expressed at low levels, corresponding to the low Ara substitution in *Arabidopsis*, it also suggests the potential for Ara transfer activity.

In this study, we overexpressed the candidate gene *AtXAT2*, an arabinosyltransferase from *Arabidopsis*, in both wild-type and *atdgux* mutant. Our results indicate that overexpression markedly enhanced the Ara substitution rate of xylan in the transgenic lines. As a result, we obtained classical materials with different xylan structural types. Through structure–function analysis of these materials, we found that xylan lacking side-chain modifications is more favorable for the preparation of xylan nanocrystals and emulsifiers with superior morphology and performance. In contrast, xylan with high arabinose substitution affects the alignment and structural characteristics of cellulose fibers, thereby enhancing cellulose degradation efficiency and improving the morphology and yield of cellulose nanocrystals. These findings provide important insights for enhancing the preparation of functional nanomaterials from different polysaccharides in biomass through precise design of xylan side chains, highlighting the significant potential of engineered lignocellulosic feedstocks in the development of bio-based products.

Materials and methods

Materials

AtXAT2 overexpression constructs were transformed into *Arabidopsis* Col.0 and *atdgux* mutants via floral dip [48]. Homozygous transgenic lines were selected through hygromycin resistance screening, with *AtXAT2* transcript levels quantified by quantitative PCR.

Biomass from Col.0, *atdgux*, and overexpression lines (*AtXAT2/Col.0*, *AtXAT2/atdgux*) was harvested from climate-controlled growth chambers at Huazhong Agricultural University. Stems were dried (55 °C), fragmented, ground through a 40-mesh sieve, and stored as biomass powder.

All chemicals (KOH, ethanol, $NaClO_2$, TFA, DMSO) were ACS-grade reagents from Sigma-Aldrich and used without purification.

Methods

Quantitative RT-PCR

Total RNA extraction was performed using the RNAprep Pure Plant Kit from Tiangen Biotech (Beijing, China). cDNA was synthesized using M-MLV Reverse Transcriptase (TaKaRa, Dalian, China). Quantitative real-time PCR (qRT-PCR) assays were conducted on a BioRad IQ5™ Real-Time PCR System (Bio-Rad Laboratories, Hercules, CA, USA) [49]. Analysis involved a minimum of three biological replicates per sample.

Preparation of xylan

Holocellulose was isolated from dry biomass powder via delignification using sodium chlorite. The biomass was treated with 8% (w/v) sodium chlorite (in 1.5% v/v acetic acid) for two 24 h cycles at room temperature in the dark. After each cycle, samples were rinsed with

ultrahigh-purity water until pH7.0. The resulting holocellulose residues were sequentially washed twice with pure methanol and twice with anhydrous acetone, air-dried overnight in a fume hood, and oven-dried at 50 °C for 2 h. Dried samples were ground through a 40-mesh sieve and stored desiccated [56].

Xylan was extracted from holocellulose with 4 M KOH. The alkaline extract was adjusted to pH5.5–6.6 using acetic acid, and xylan was precipitated by adding ethanol to 75% (v/v). Pellets obtained by centrifugation were washed with 70% (v/v) ethanol and lyophilized [34]. The use of 4 M KOH is a standard and necessary method for the efficient extraction of xylan tightly integrated into the secondary cell wall matrix [50]. It is important to note that while these conditions hydrolyze alkali-labile ester-linked substitutions (such as acetyl groups or ferulate cross-links), the glycosidic linkages attaching both arabinose and glucuronic acid side chains to the xylan backbone are stable under alkaline extraction [51]. Consequently, this approach is robust for the comparative analysis of the substitution patterns of these major side chains across different genotypes.

Quantitative analysis of monosaccharides and uronic acids

The polysaccharides dissolved in 2.5 mL TFA (2 M) were heated in a sealed tube at 121 °C in an autoclave (15 psi) for 1 h. Myo-inositol (200 μg) was added as the internal standard. The supernatant was dried under vacuum at 38 °C to remove TFA.

Derivatization of monosaccharides: distilled water (800 μL) and a freshly prepared solution of $NaBH_4$ (400 μL, 100 mg/mL in 6.5 M aqueous NH_3) were added to each sample. The sample was capped, mixed well, and incubated at 40 °C for 30 min. Excess $NaBH_4$ was decomposed by adding acetic acid (800 μL). 400 μL of the sample was then moved into a 25-mL glass tube. Acetic anhydride (4 mL) was added to the tube and the solution was mixed again. Then 1-methylimidazole (600 μL) was added. After mixing, the sample was allowed to stand for 10 min. Excess acetic anhydride was decomposed by adding distilled water (10 mL). Then dichloromethane (3 mL) was added, mixed gently, centrifuged (2,000 g, 10 s) for phase separation. After removing the upper phase, the sample was washed with distilled water (3 × 20.0 mL). The collected lower phase was dehydrated by adding anhydrous sodium sulfate and stored at −20 °C until analyzed by GC–MS (SHIMADZU GCMS-QP2010 Plus) [52, 53].

For uronic acid quantification, crude cell walls were incubated in 5.0 ml of 0.5% (w/v) ammonium oxalate solution at 100 °C for 1 h. Supernatants (designated as pectic polysaccharides) were analyzed by UV–VIS spectrometry (V-1100D, Shanghai MAPADA). All assays included three biologically independent replicates [54].

Characterization of hemicellulose

FTIR spectroscopy was performed to observe the structural constituents and chemical linkages in the xylan and xylan nanocrystals. A Perkin-Elmer spectrophotometer (NEXUS 470, Thermo Fisher Scientific, Waltham, MA, USA) was used to qualitatively monitor the samples through spectroscopic grade potassium bromide (KBr) pellet. The well-dried biomasses were finely powdered to reduce scattering losses and deformations in the absorption band. The samples (2–4 mg) were dispersed in KBr at the weight ratio of 1:100 and subsequently pressed to produce a transparent pelletized disc by applying 1 Mpa pressure for at least 2 min [49]. The pelletized disc samples were positioned in the path of IR light and the spectra were recorded in absorption mode over 32 scans at a resolution of 4 cm^{-1} in the range of 4000 to 400 cm^{-1} region [55]. XRD was performed on a Rigaku Ultima IV diffractometer with curved detector (Rigaku Americas) operating at 40 kV and 40 mA (Cu Kα $\lambda = 1.5418$ Å). Continuous line scans with $\theta/2\theta$ geometry covered 5–60° 2θ range in dual sample orientations [30, 56]. Elemental composition and binding energies were characterized by XPS (Thermo Scientific K-Alpha). HSQC NMR spectra were acquired in HSQCGE mode with 64 scans. Data processing employed MestReNova software [34].

Preparation and characterization of XNCs

The xylan precipitate was dispersed in deionized water as previously described. Aqueous xylan suspensions underwent sonication (15 W/mL, 40 min) using a JY99-IIDN ultrasonic homogenizer (Ningbo Xinzhi Biological, China) to obtain stable xylan nanocrystal (XNC) colloids [10]. Diluted dispersions were negatively stained with phosphotungstic acid prior to morphological characterization by TEM [10, 13].

Preparation and characterization of Pickering emulsion

To assess XNCs' impact on Pickering emulsion properties, XNCs derived from diverse xylan sources were utilized. Primary oil-in-water (O/W) emulsions were formulated by blending 10 v% dodecane with 90 v% aqueous phase. These pre-emulsions were then homogenized using a high-shear mixer (11,000 rpm, 1 min) to generate stabilized Pickering emulsions [54, 57].

Morphology of Pickering emulsions was observed using an Olympus BX61 optical microscope. The surface charge of the Pickering emulsions was determined using a dynamic light scattering/electrophoresis instrument (Zetasizer Nano ZS, Malvern Instruments, Worcestershire, UK) [54, 58]. The interfacial tension of Pickering

emulsions prepared with different xylan nanocrystals (XNCs) was tested using a drop shape analyzer rheometer (Tracker Teclis/IT Concept, France) at 25 °C [54]. According to the method of Hu, the emulsifying activity was tested using a UV–VIS spectrophotometer (Shanghai Mapada Instrument Co., Ltd., Shanghai, China) [13]. The stability of Pickering emulsions was characterized through evaluating creaming index (ECI%) and droplet size [13]. ECI was calculated by using the following formula:

$$ECI = H_A / H_T \times 100\%$$

where H_A is the height of the cream layer and H_T is the total height of the emulsions.

Measurement of cellulose features

Crystalline cellulose extraction employed 0.1 g biomass powder with 5 mL acetic acid–nitric acid–water (8:1:2, v/v/v). Cellulose content was quantified using a V-1100D UV–VIS spectrophotometer (Shanghai MAPADA) [59], while substrate polymerization degree (DP) was determined by viscometry [60].

Alkaline (NaOH) pretreatment and sequential enzymatic hydrolysis were performed as previously described by Fan et al. [61]. Specifically, biomass powder was incubated with 6 mL of 1% (w/v) NaOH under shaking (150 rpm) at 50 °C for 2 h. After centrifugation at 3000 × g for 5 min, the pretreated biomass residues were incubated with the mixed-cellulase enzymes as described above. All experiments were performed in biological triplicates.

Preparation and observation of cellulose microfibrils

The base stems tissues of 7-week-old plants were sectioned into 60-μm slices using a vibrating microtome (VT1000S, Leica). The sections underwent de-lignin with 8% sodium chlorite containing 1.5% acetic acid [62], were washed with ultrapure water to achieve neutral pH, and then laid flat on mica sheets to dry naturally before atomic force microscopy (AFM) observation.

AFM imaging was performed using a Pointprobe™ NCHR-20 probe (NanoWorld, Switzerland), which has a spring constant of 45 N/m and a tip radius of 8 nm, with a scanning area of 2 μm × 2 μm. The orientation of cellulose fibers was analyzed from the AFM images using NanoScope image analysis software (version 1.90). Orientation distributions were quantified and presented as frequency percentages in polar histograms [19].

Generation of cellulose nanocrystals in vitro

Crude cellulose underwent sulfuric acid hydrolysis for CNC production. Prior to hydrolysis, samples were pretreated with 8% $NaClO_2$ following established protocols [62]. For acid digestion, 0.1 g dried cellulose was immersed in 2 mL of 64% (w/w) H_2SO_4 at 45 °C for 1.5 h under 40 kHz ultrasonication. The reaction was quenched by tenfold dilution with ice-cold distilled water, followed by centrifugation (6,000 × g, 5 min) for acid removal. The pellet residues were re-suspended in 45 mL of ultrapure water and centrifuged again (6,000 × g, 5 min), allowing the nanocrystals to evenly suspend in the supernatant. The upper layer containing the nanocrystals was collected, dialyzed (MWCO: 14 kDa, 3 days), and then sonicated (15 min) to prevent aggregation. The resultant dispersion was diluted to 0.001% (w/w) with ultrapure water and vortex-mixed prior to AFM analysis. The CNCs were observed using a MultiMode 8-HR Scanning Probe Microscope (Bruker MM-SPM) equipped with a NanoScope V controller (Veeco). Imaging was performed with a ScanAsyst-Air probe (Bruker) over a 1 μm × 1 μm area at a resolution of 512 × 512 pixels^2. To ensure repeatability, at least three independent replicates were measured. The dimensions of the CNCs (length/diameter) were determined from AFM topographical profiles.

The yield of nanocrystals was calculated by collecting all of the upper layer nanocrystal suspension, freeze-drying it, weighing it, and calculating it as a percentage of the initial cellulose.

Statistical analysis

All data were processed using SPSS 17.0 (IBM, USA). Parameter correlations used Spearman's rank; pairwise comparisons applied Student's *t*-test.

Results

Genetic engineering enables precise modification of xylan's side-chain in *Arabidopsis*

Arabidopsis stem xylan is thought to be decorated with glucuronic acid (GlcA) side chains rather than arabinose (Ara). This unique glycosylation profile makes it an ideal "blank slate" acceptor for in vitro assays aimed at evaluating the arabinofuranosyl transferase activity of GT61-family candidates from a variety of plant species [36, 39]. However, introducing heterologous genes into the background material itself may introduce other unknown variables. Therefore, we focused on *AtXAT2* (*At03g18170*), one of the two members in clade A of the *Arabidopsis* GT61 family, which is highly homologous to the previously reported arabinose transferase OsXAT2 in rice and is primarily expressed in stems (Fig. S1, Fig. S2). We overexpressed *AtXAT2* in both wild-type *Arabidopsis* and the *atdgux* mutant, which is a double gene mutant obtained by crossing the *GUX1* and *GUX2* T-DNA insertion homozygous mutants, and consequently lacks GlcA side chains [39]. Compared to

the background lines Col.0 and *atdgux*, the expression levels of the *AtXAT2* gene are significantly elevated in the *AtXAT2/Col.0* and *AtXAT2/gux* lines, respectively, while no significant difference is observed between Col.0 and *atdgux* (Fig. 1A). Monosaccharide composition analysis indicated a marked increase in Ara content in the transgenic lines, corresponding to their respective genetic backgrounds (Fig. 1B, Table 1). Additionally, the uronic acid measurements demonstrated a significant reduction in uronic acid levels in both the *atdgux* mutant and *AtXAT2/atdgux* lines compared to Col.0 (Fig. 1C). The findings were further validated using 2D-HSQC NMR analysis (Fig. 2). Hemicellulose extracted from holocellulose was analyzed using ^{1}H–^{13}C HSQC NMR. The results showed that in the Col.0 and *AtXAT2/Col.0* lines (Fig. 2A, B), there were prominent peaks for GlcA (U_1: 97.4/5.05; U_4: 82.2/2.97; U_5: 71.2/4.11). In contrast, the peaks for U_1 and U_4 were absent in the *atdgux* mutants and *AtXAT2/atdgux* lines (Fig. 2C, D), indicating that the xylan from *atdgux* and *AtXAT2/atdgux* lacked GlcA modification. Additionally, in the 2D-HSQC NMR analysis of the *AtXAT2/Col.0* and *AtXAT2/atdgux* transgenic lines (Fig. 2B, D), an extra peak for Ara was observed (A_1: 110.9/4.72; A_4: 84.4/4.16), suggesting that the xylan from the *AtXAT2/Col.0* and *AtXAT2/atdgux* transgenic lines was modified with Ara.

XPS (X-ray photoelectron spectroscopy) is a technique used to analyze the elemental composition and chemical states on the surface of materials. Changes in the C–C and C–O–C peaks in the C1s spectrum of xylan, as well as the changes in the C–O and C=O peaks in the O1s spectrum, can provide some insight into its chemical structure. To further confirm the features of xylan across the different materials, XPS analysis was performed on xylan obtained through alkaline extraction and alcoholic precipitation. The results show that, compared with Col.0 and *AtXAT2/Col.0*, the C–C peak in the C1s spectrum of xylan from *atdgux* and *AtXAT2/atdgux* sources is elevated, while the O=C–O peak corresponding to the carboxyl structure of uronic acids is reduced (yellow peak), indicating a decrease in the degree of carboxylic acid groups (Fig. 3A, B). Additionally, compared to Col.0, the *AtXAT2/Col.0* line shows a decrease in the C-O component of the O1s spectrum (Fig. 3C), and a similar trend is observed between *AtXAT2/atdgux* and *atdgux*. This reduction, coupled with the corresponding attenuation of the C–O–C signal in the C1s spectrum, supports the conclusion that there are structural differences in the xylan derived from the four different sources.

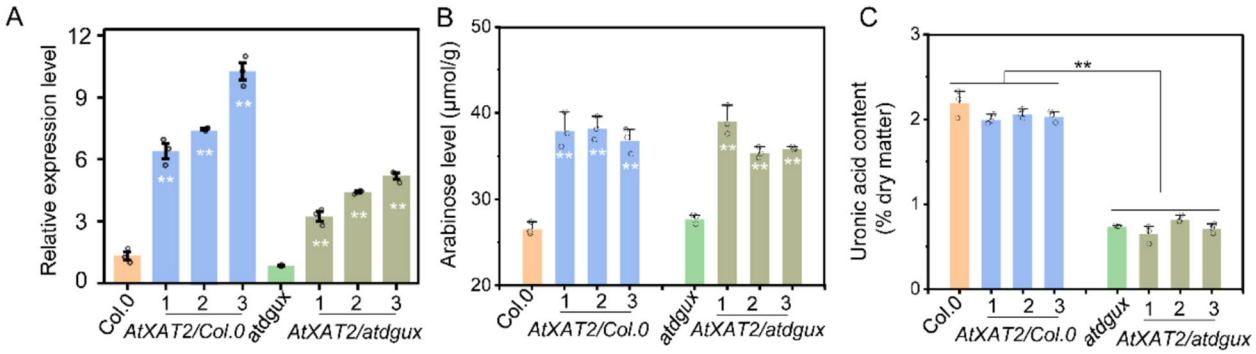

Fig. 1 Quantitative analysis of Ara and glucuronic acid content in hemicellulose. **A** Expression levels of *AtXAT2*. **B**, **C** Measurement of Ara and glucuronic acid contents. Significant differences were determined by two-tailed Student's *t*-test: $^{**}p < 0.01$, $^{*}p < 0.05$. Data as means ± SD ($n = 3$)

Table 1 Monosaccharides composition of 4 M KOH fractions

Sample	Monosaccharides contents (% of total)							Ara/Xyl (%)
	Ara	Xyl	Rha	Fuc	Man	Glc	Gal	
Col.0	2.68 ± 0.12	77.24 ± 4.39	2.44 ± 4.26	0.64 ± 0.02	4.55 ± 0.15	4.57 ± 0.81	8.52 ± 0.68	3.47 ± 0.01
AtXAT2/Col.0	3.73 ± 0.45**	76.33 ± 3.45	2.84 ± 1.09	0.85 ± 0.01	4.28 ± 0.32	4.84 ± 0.17	7.13 ± 0.37	4.89 ± 0.36**
atdgux	2.79 ± 0.07	76.20 ± 5.24	3.18 ± 1.66	0.74 ± 0.02	4.52 ± 0.34	4.95 ± 0.45	7.66 ± 0.41	3.67 ± 0.17
AtXAT2/atdgux	3.87 ± 0.05**	76.09 ± 2.08	3.08 ± 1.45	0.89 ± 0.03	4.47 ± 0.17	4.27 ± 0.21	7.31 ± 0.30	5.08 ± 0.07**

Data as means ± SD ($n = 3$), $^{**}p < 0.01$

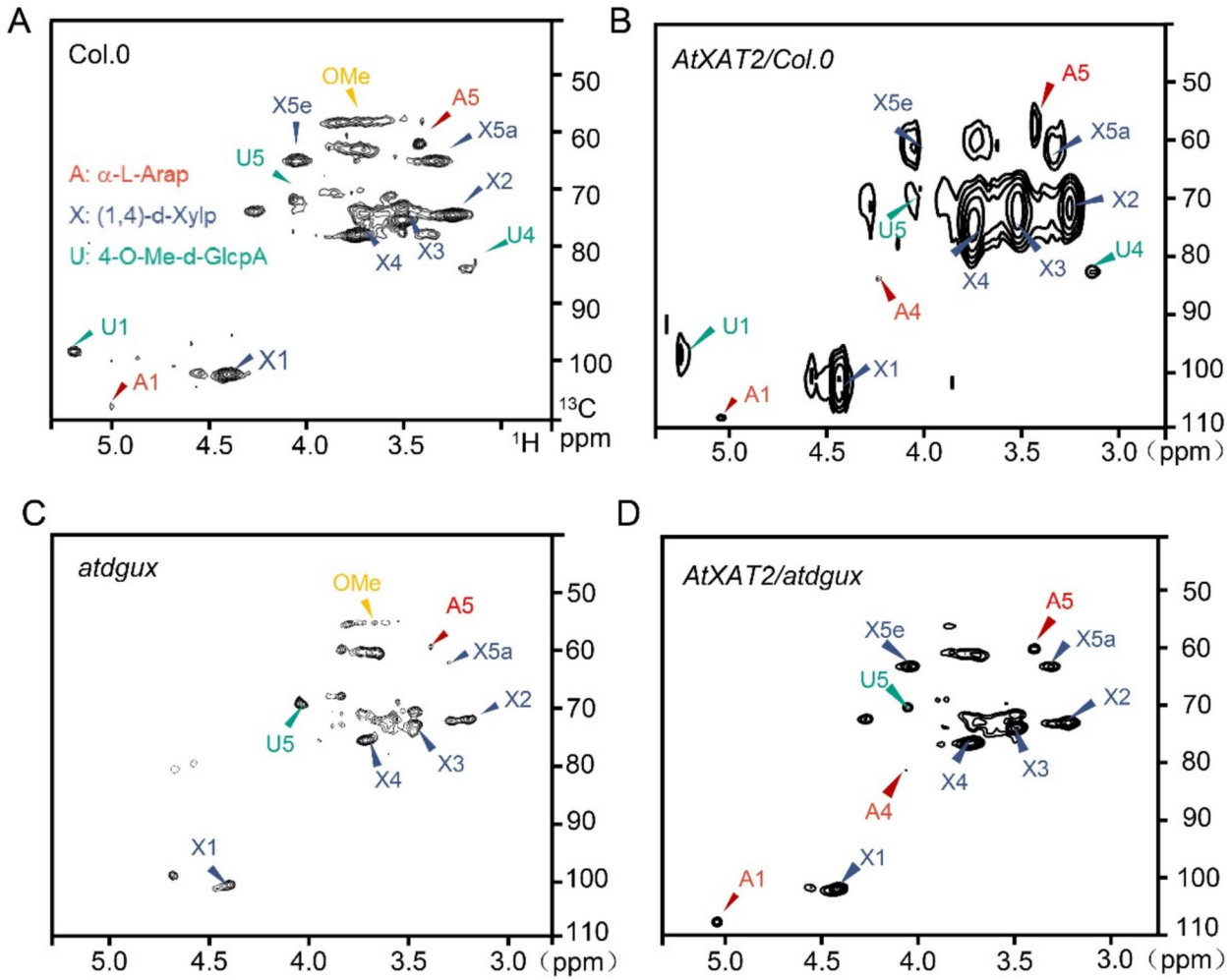

Fig. 2 HSQC-NMR spectra of xylan substrates in *Arabidopsis* transgenic lines and mutants, **A** Col.0. **B** *AtXAT2/Col.0*. **C** *atdgux*. **D** *AtXAT2/atdgux*

The absence of the uronic acids peak in *atdgux* and *AtXAT2/atdgux,* along with the increased Ara peak in the *AtXAT2/Col.0* and *AtXAT2/atdgux* transgenic lines, supports our hypothesis that the xylan structure can be precisely engineered. This strategic modification not only enhances our understanding of the biochemical roles of specific sugar modifications but also provides a foundation for future studies aimed at elucidating how these modifications affect cell wall properties, mechanical strength, and properties of biopolymers. In summary, we have successfully developed a targeted engineering approach that produces representative genetic materials with distinct xylan structures: *AtXAT2/Col.0* lines enriched in both GlcA and Ara side chains, Col.0 enriched in GlcA, *AtXAT2/atdgux* transgenic lines enriched in Ara, and *atdgux* mutants lacking branching modifications.

Low-substituted xylan favors nanocrystals production with exceptional properties

XNCs, characterized by their unique nanoscale structure, exhibit significant application potential across various fields, including food, pharmaceuticals, and materials science [63–66]. In the food industry, these nanocrystals can function as effective emulsifiers and thickeners, enhancing the texture and stability of products such as dairy items, condiments, and beverages [67–69]. Furthermore, their distinctive chemical structure and diverse side-chain modifications enable hemicellulose to effectively reduce the surface tension of liquids, stabilizing oil–water mixtures and forming homogeneous emulsions. Due to their biocompatibility and biodegradability, hemicellulose emulsifiers also demonstrate promising applications in the development of cosmetics and eco-friendly materials [70, 71].

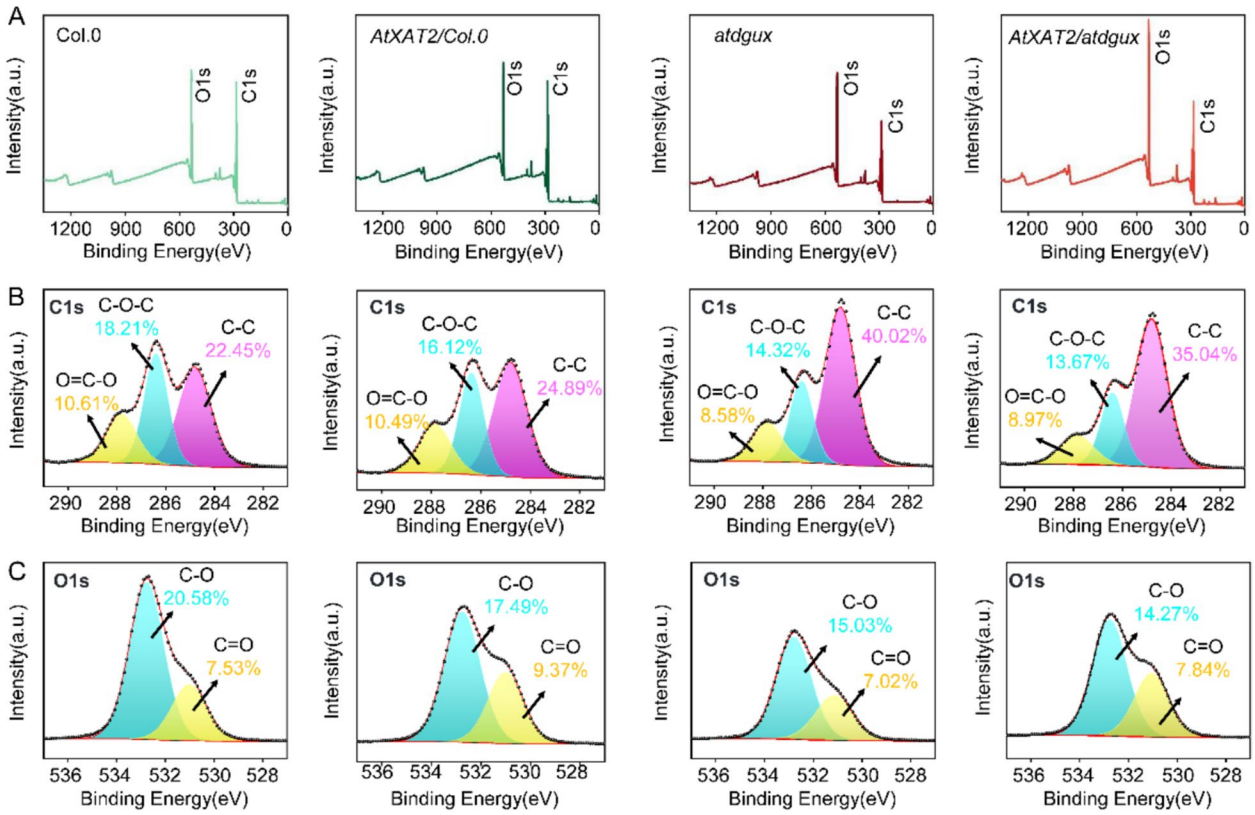

Fig. 3 XPS profiling of xylan substrates in *Arabidopsis* transgenic lines and mutants. **A** XPS spectra profile of the xylan. **B**, **C** High-resolution XPS spectrum at C1s region, O1s region

To analyze the relationship between xylan side-chain variations and the performance of nanocrystals and emulsifiers, we prepared both from xylans with different structural types and conducted comparative analyses. Hemicellulose extracted using 4 M KOH was neutralized with acetic acid and precipitated in 70% ethanol, resulting in the formation of crude, deacetylated xylan [34]. Aqueous suspensions of each xylan were sonicated for 40 min at 20 kHz/320 W, then aged at 4 °C for 72 h to yield stable xylan nanocrystal

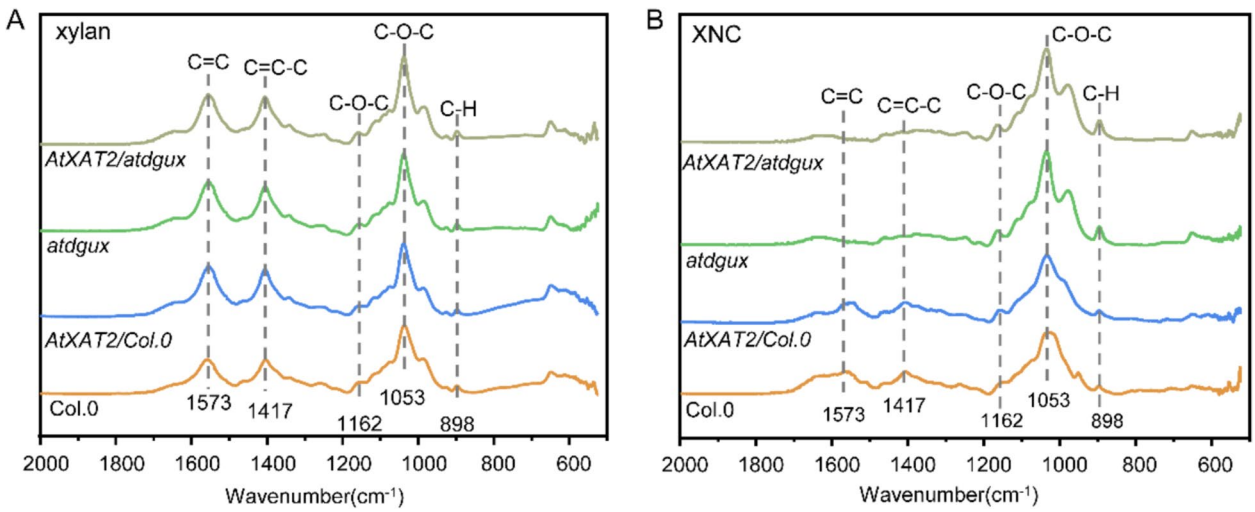

Fig. 4 FT-IR spectroscopic profiling. **A** Xylan and **B** XNCs generated from *Arabidopsis* transgenic lines and mutants

(XNC) colloids (Fig. S3). FTIR analysis shows that both alkali-extracted xylan and XNCs exhibit differences at the xylan characteristic peaks of 1000–1200 cm^{-1}, indicating variations in the chemical structures of XNCs sourced from four different origins (Fig. 4). After dilution, the resulting XNC dispersions were negatively

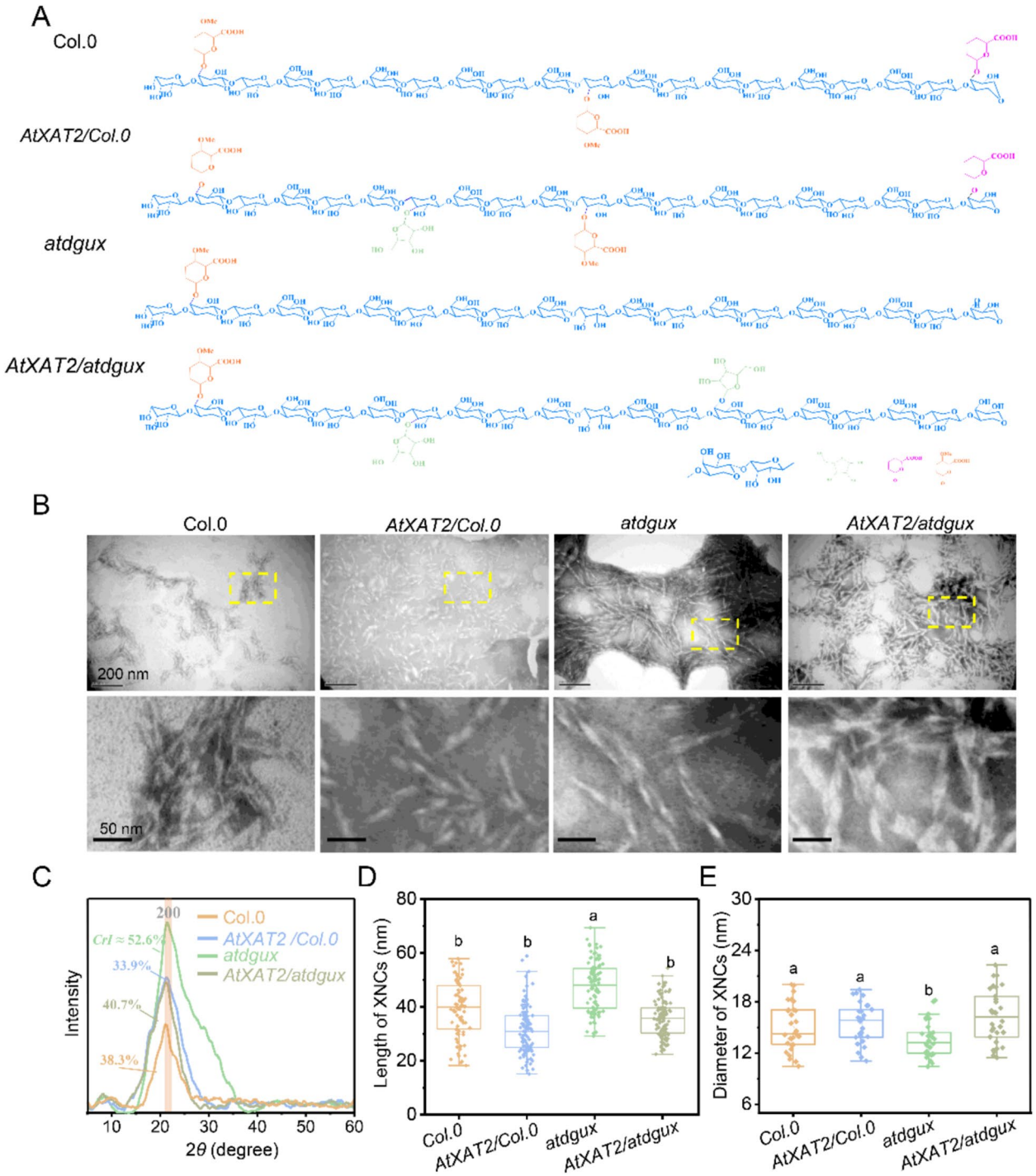

Fig. 5 Characterization of the XNCs derived from *Arabidopsis* transgenic lines and mutants. **A** Schematic representation of key xylan structural motifs. **B** Representative TEM images of XNCs, scale bar, 200 nm, 50 nm. **C** XRD pattern of XNCs. **D**, **E** Measurement of XNCs morphology. Length (**D**) and diameter (**E**) distributions were determined from 50 randomly selected XNCs for length and 30 for diameter; different letters on each column were significantly different at $P < 0.05$

stained with phosphotungstic acid and imaged by transmission electron microscopy (TEM), revealing well-defined nanocrystals (Fig. 5). Nanocrystals prepared from xylans bearing different side-chain modifications displayed distinct differences and patterns (Fig. 5A). Notably, the nanocrystals derived from *atdgux* displayed a more ordered arrangement, while those from *AtXAT2/atdgux* were characterized by a more "rounded" and "looser" appearance (Fig. 5B). XRD analysis indicates that the xylan nanocrystals exhibit a distinct characteristic peak intensity at 21.7° (200). The crystallinity calculations show that the crystallinity index (*CrI*) for *atdgux* is relatively high at 52.5%, while the *CrI* values for Col.0, *AtXAT2/Col.0*, and *AtXAT2/atdgux* are 38.3%, 33.9%, and 40.7%, respectively (Fig. 5C). Measurements of the length and diameter showed that the XNCs from *atdgux* exhibited larger lengths and smaller diameters compared to the other three groups, indicating a morphology closer to rod-shaped (Fig. 5D and E). These findings align with our previous study on sorghum [34], demonstrating that side-chain modifications of xylan strongly influence nanocrystal formation. Furthermore, the results suggest that xylans with lower degrees of modification are more likely to yield stable, elongated rod-shaped nanocrystals.

The abundance of hydroxyl groups renders xylan nanoparticles intrinsically hydrophilic, making them ideal candidates for Pickering emulsifiers. We therefore prepared Pickering emulsions using dodecane as the oil phase and XNCs from different genetic backgrounds as the sole stabilizers (Fig. S4). After 3 days of quiescent storage, optical microscopy revealed uniformly dispersed droplets (Fig. 6A). Diameter measurements using ImageJ revealed that the droplet sizes of all four emulsions ranged from 5 to 40 μm (Fig. 6A and B). Emulsions stabilized by GlcA-enriched nanocrystals from Col.0 produced the smallest droplets, whereas those stabilized by Ara-enriched nanocrystals from *AtXAT2/atdgux* exhibited a significantly higher proportion of larger droplets (Fig. 6B). The creaming index serves as a quantitative proxy for emulsion stability. The stability of Pickering emulsions was monitored daily over a 7-day period at room temperature. Compared to the transformation backgrounds, the

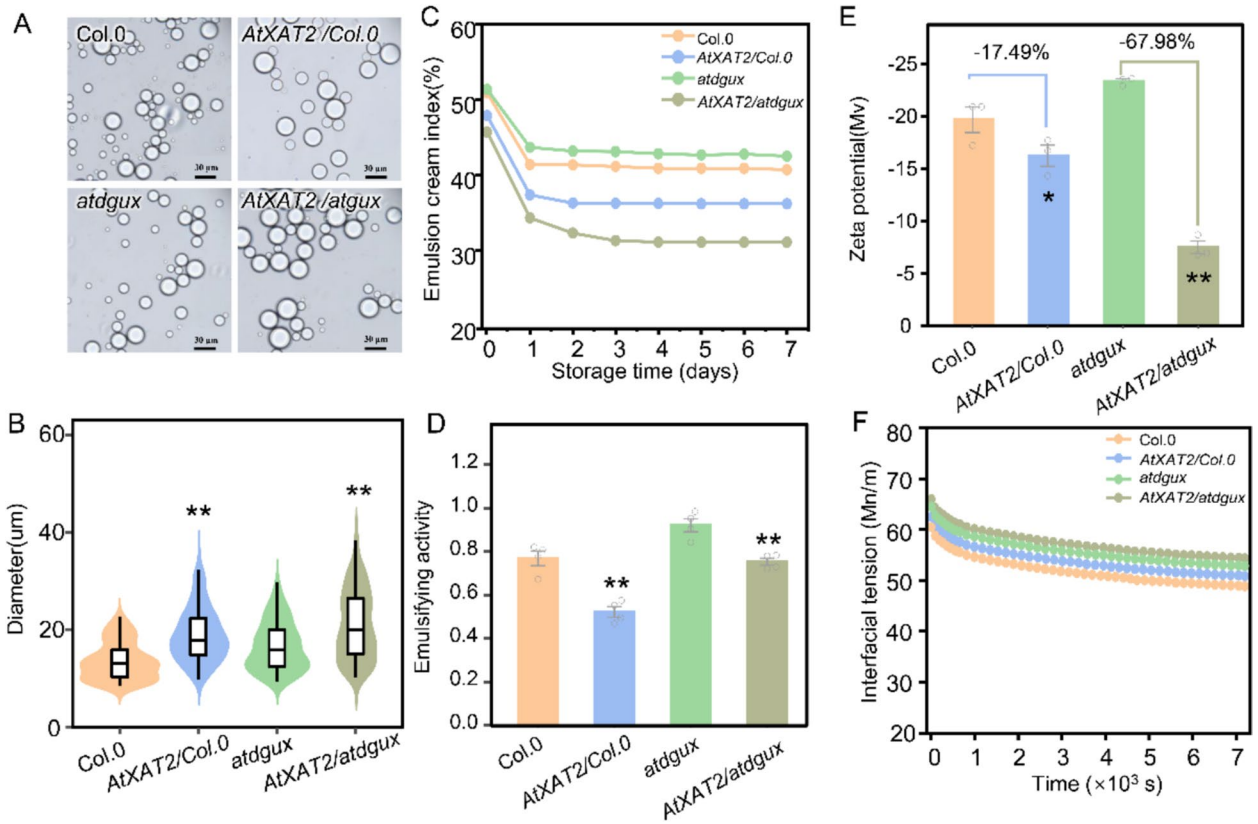

Fig. 6 Characterization of Pickering emulsions stabilized by XNCs from *Arabidopsis* transgenic line and mutants. **A** Representative optical micrographs; scale bar, 30 μm. **B** Particle size distribution of the Pickering emulsions ($n = 100$). **C**, **D** Emulsion creaming index and emulsifying activity (n = 4). **E** Zeta potential ($n = 3$). **F** Dynamic interfacial tension at the oil–water interface versus time. Significant differences between the raw materials and mutants were determined using two-tailed Student's *t*-test: $^{**}p < 0.01$, $^{*}p < 0.05$

emulsions derived from *AtXAT2/Col.0* and *AtXAT2/atdgux* displayed higher creaming indices (Fig. 6C), reduced emulsifying activity (Fig. 6D), lower zeta potential (Fig. 6E), and decreased surface tension (Fig. 6F). Collectively, these findings indicate that xylans devoid of Ara side chains provide enhanced emulsion stability.

Xylan is a structural polysaccharide naturally present in plant cells. Owing to its environmentally friendly, renewable, and biodegradable characteristics, it has garnered significant attention in the development of hemicellulose-based functional polymer materials. In recent years, various physical and chemical modification methods have been employed to prepare xylan-based nanoparticles. In this study, we precisely targeted the side-chain structure of xylan and successfully utilized a mild ultrasonic method to prepare nanocrystalline particles with different sizes and surface properties. The XNCs from different sources have controllable size distributions and stable surface structures, which enable them to adsorb at the oil–water interface and form highly stable Pickering emulsions. Our study results show that xylans with Ara modifications do not have a clear advantage in the preparation of emulsifiers. This may be because, unlike GlcA, which can enhance molecular polarity, Ara increases the steric hindrance but does not significantly alter the molecular polarity.

Xylan patterning modulates cellulose microfibrils assembly and digestibility

Xylan is cross-linked with lignin via Ara branches to form lignin–carbohydrate complexes, while it also interacts closely with the amorphous regions of cellulose [13, 20]. The structure of xylan has a significant impact on the structural properties of cellulose and the remodeling of the cell wall ultrastructure [20]. To investigate the impact of different xylan side-chain modifications on cellulose structure, basal stem sections from the bolting stage of each plant line were collected to prepare 80-μm-thick slices. These slices were treated with 8% sodium chlorite to remove lignin, and then cellulose microfibrils were observed in situ using atomic force microscopy (AFM) (Fig. 7A, B). Cellulose morphology analysis revealed that, relative to Col.0, both the *atdgux* mutant and the transgenic lines displayed marked alterations in cellulose

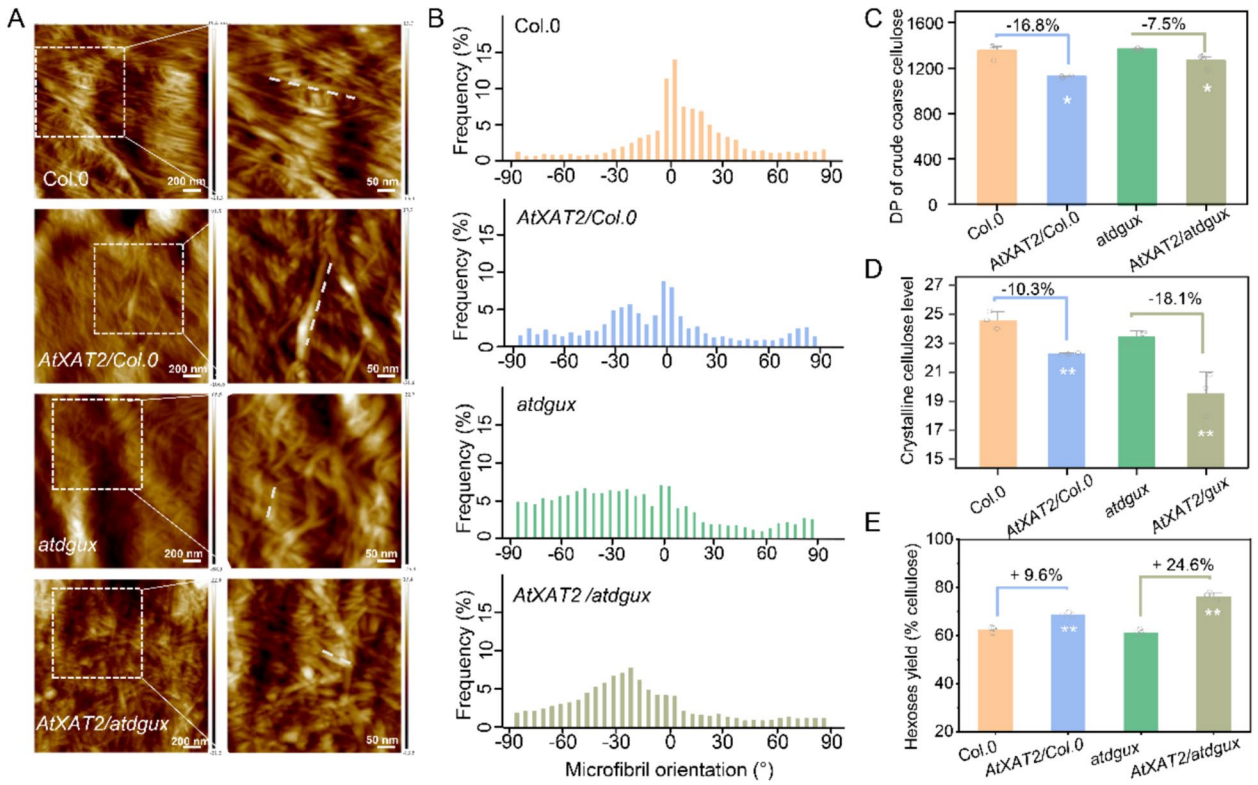

Fig. 7 Characterization of cellulose microfibrils from *Arabidopsis* transgenic lines and mutants. **A** AFM observation of cellulose microfibrils, scale bar as 200 nm, 50 nm, the areas in the white boxes are magnified in the lower images. **B** Orientation distribution profiles of cellulose microfibrils analyzed with SOAX software ($n \geq 250$ snakes). **C**–**E** Degree of polymerization (DP) (**C**), crystalline cellulose level (**D**), and hexoses yield of cellulose microfibrils (**E**). Significant differences between the raw materials and mutant were determined using two-tailed Student's *t*-test: $^{**}p < 0.01$, $^{*}p < 0.05$. Data as means ± SD ($n = 3$)

microfibril shape and alignment angles. Notably, the *atdgux* mutant displayed severe, disordered aggregation and misalignment of cellulose microfibrils, demonstrating that these side-chain decorations are indispensable for sustaining cell wall ultrastructure and the precise, orderly assembly of cellulose (Fig. 7B). To further evaluate the impact of xylan branching patterns on the cellulose features and saccharification efficiency, we measured the degree of polymerization (DP) and crystallinity index (CrI) of cellulose. Interestingly, the cellulose DP and CrI of *atdgux* showed no significant difference from those of Col.0. However, in *AtXAT2* overexpressing transgenic lines, cellulose DP decreased by 16.8% and 7.5% relative to the transformation backgrounds (Fig. 7C). Additionally, the cellulose crystallinity declined by 10.3% and 28.5%, respectively (Fig. 7D). Furthermore, saccharification efficiency analysis under 1% KOH treatment revealed that the *AtXAT2* overexpressing lines exhibited increases in saccharification efficiency of 9.6% and 24.6% compared to their transformation backgrounds, respectively (Fig. 7E). Overall, these results indicate that xylan side-chain modifications have a significant impact on the polymerization mode and alignment angles of cellulose, as well as saccharification efficiency. In particular, Ara side chains are crucial for the stability of the cellulose ultrastructure, while glucuronic acid side chains tend to influence the alignment and aggregation of cellulose microfibrils. This may be due to the close contact and interaction between Ara and the amorphous regions of cellulose [15, 72].

Ara side chain of xylan optimizes the size and yield of cellulose nanocrystals

Cellulose nanocrystals are increasingly utilized in biocomposites, biomedicine, food packaging, and energy applications due to their biodegradability, biocompatibility, high crystallinity, and exceptional mechanical properties [63]. This makes them a focal point in materials science and nanotechnology. The structural characteristics of cellulose significantly influence the morphology and yield of cellulose nanocrystals [62]. The H_2SO_4 treatment demonstrated its effectiveness in removing amorphous cellulose chains from the surfaces of entire cellulose microfibrils. By employing 64% H_2SO_4 (w/w) at 45 °C to treat holocellulose extracted from various materials, we successfully generated well-defined cellulose nanocrystals (CNCs) in vitro (Fig. S5). These cellulose nanocrystals were subsequently analyzed using atomic force microscopy (AFM), revealing that the CNCs derived from all materials exhibited a spindle-shaped morphology (Fig. 8A). A total of 100 CNCs were randomly selected from each material to measure and statistically analyze their length and diameter. The results showed that, compared to the transformation backgrounds, the length and diameter of cellulose nanocrystals (CNCs) in the overexpressing lines were significantly reduced (Fig. 8B, C). Furthermore, the yield of isolated CNCs was evaluated by processing the upper layer of the CNC suspension through freeze-drying followed by weighing. This yield was expressed as a percentage of the initial cellulose content. The analysis revealed increases of 13.8% and 6.7% in the AtXAT2 overexpressing lines compared to their respective transformation background controls (Fig. 8D). These observations may be attributed to alterations in the xylan side-chain structure, which in turn lead to differences in the cross-linking methods and tightness with cellulose. Such changes further induce variations in the ultrastructure and aggregation patterns of cellulose [72]. In summary, the plant cell wall is a complex yet highly ordered network composite. By precisely tuning the structure of xylan, it is possible to not only directionally design the functional value of xylan itself, but also simultaneously modify the structural characteristics of cellulose. This dual approach can enhance enzymatic hydrolysis efficiency, optimize nanocrystal morphology, increase yield, and realize other value-added benefits.

Conclusions

In this study, the side chain substitution of xylan was precisely modified by overexpressing the *AtXAT2* gene in the wild type (Col.0) and the glucuronic acid-deficient mutant (*atdgux*), achieving precise design of the xylan structure. This precise engineering deepens our understanding of the biochemical roles of specific sugar modifications in xylan and their impact on cell wall properties. Our findings indicate that xylan with customized side-chain modifications can yield XNCs with superior emulsifying properties, demonstrating their potential application value in food, pharmaceuticals, and environmentally friendly materials.

Further analysis revealed that changes in the xylan structure had a profound impact on cellulose properties. The overexpressing lines exhibited a disordered arrangement of cellulose microfibrils, reduced polymerization degree, and decreased crystalline cellulose content. These alterations enhanced cellulose digestibility, as evidenced by higher sugar yields from enzymatic hydrolysis in the *AtXAT2/Col.0* and *AtXAT2/atdgux* lines compared to the background, respectively. Additionally, cellulose nanocrystals extracted from *AtXAT2/Col.0* and *AtXAT2/atdgux* showed smaller sizes and higher yields, highlighting the critical role of xylan structure in modulating the structural characteristics and functions of cellulose. Overall, our work not only elucidates the intricate relationship between xylan structure and cellulose properties, but also provides a foundation for future research

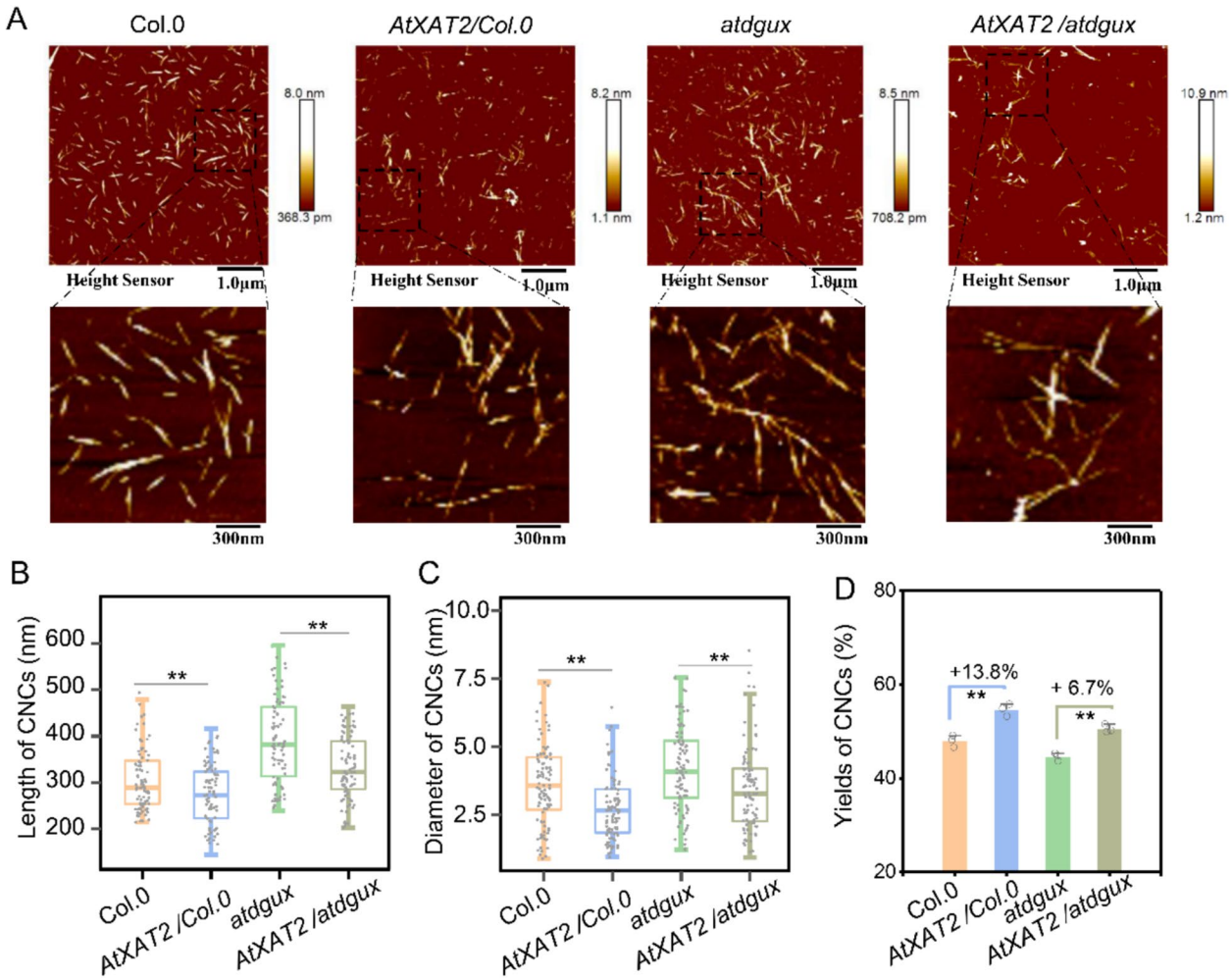

Fig. 8 Characterization of cellulose nanocrystals (CNCs) isolated from *Arabidopsis* transgenic lines and mutants. **A** Representative AFM images of CNCs, scale bar, 1 μm, 300 nm, regions within the black boxes are enlarged in the bottom row. **B**–**D** Quantitative analysis of CNC length (**B**), diameter (**C**), and yield (**D**). 100 CNCs were randomly measured across three biologically independent replicates. Statistical significance was evaluated using a two-tailed Student's *t*-test: $^{**}p < 0.01$, $^{*}p < 0.05$

aimed at optimizing plant polysaccharides for various industrial applications.

Supplementary Information

The online version contains supplementary material available at https://doi.org/10.1186/s13068-026-02739-5.

Supplementary material 1.
Supplementary material 2.
Supplementary material 3.
Supplementary material 4.
Supplementary material 5.

Author contributions

Sunfang Li: Methodology, Investigation, Formal analysis, Writing-original draft. Min Li: Methodology, Investigation, Writing-original draft. Hailang Wang: Conceptualization, Methodology, Validation. Tianqi Li: Methodology, Investigation. Zhen Hu: Methodology, Funding acquisition. Yanting Wang: Methodology. Peng Chen: Methodology. Zhaosheng Kong: Conceptualization, Supervision. Liangcai Peng: Conceptualization, Supervision. Youmei Wang: Conceptualization, Funding acquisition, Supervision, Writing-review & editing.

Funding

This work was in part supported by the National Natural Science Foundation of China (32370286, 32400212, 32241038), the National Key Research and Development Program of China (2023YFD1202704), the Young Science & Technology Leadership Program of Shanxi Agricultural University (2023YQPYGC04).

Data availability

No datasets were generated or analysed during the current study.

Declarations

Ethics approval and consent to participate

Not applicable.

Consent for publication
Not applicable.

Competing interests
The authors declare no competing interests.

Author details
[1]Shanxi Hou Ji Laboratory, College of Agriculture, Shanxi Agricultural University, Taiyuan 030000, China. [2]Key Laboratory of Fermentation Engineering (Ministry of Education), Hubei Key Laboratory of Industrial Microbiology, Biomass and Bioenergy Research Center, School of Life and Health Sciences, Hubei University of Technology, Wuhan 430068, China. [3]College of Plant Science and Technology, Huazhong Agricultural University, Wuhan 430070, China.

Received: 24 September 2025 Accepted: 4 January 2026
Published online: 23 January 2026

References

1. Rao J, Lv Z, Chen G, Peng F. Hemicellulose: structure, chemical modification, and application. Prog Polym Sci. 2023;140:101675. https://doi.org/10.1016/j.progpolymsci.2023.101675.
2. Oliveira DM, Mota TR, Salatta FV, Marchiosi R, Gomez LD, McQueen-Mason SJ, et al. Designing xylan for improved sustainable biofuel production. Plant Biotechnol J. 2019;17(12):2225–7. https://doi.org/10.1111/pbi.13150.
3. Urtiga SCdC, Alves VMO, Melo CdO, Lima MNd, Souza E, Cunha AP, et al. Xylan microparticles for controlled release of mesalamine: production and physicochemical characterization. Carbohydr Polym. 2020;250:116929. https://doi.org/10.1016/j.carbpol.2020.116929.
4. Liao G, Sun E, Kana EBG, Huang H, Sanusi IA, Qu P, et al. Renewable hemicellulose-based materials for value-added applications. Carbohydr Polym. 2024;341:122351. https://doi.org/10.1016/j.carbpol.2024.122351.
5. Naidu DS, Hlangothi SP, John MJ. Bio-based products from xylan: a review. Carbohydr Polym. 2018;179:28–41. https://doi.org/10.1016/j.carbpol.2017.09.064.
6. Zhang Y, Wang L, Zhang H, Rosqvist E, Lastusaari M, Peltonen J, et al. Crystalline nanoxylan from hot water extracted wood xylan at multi-length scale: molecular assembly from nanocluster hydrocolloids to submicron spheroids. Carbohydr Polym. 2024;335:122089. https://doi.org/10.1016/j.carbpol.2024.122089.
7. Ma YS, Morozova SM, Kumacheva E. From nature-sourced polysaccharide particles to advanced functional materials. Adv Mater. 2024;36(23):2312707. https://doi.org/10.1002/adma.202312707.
8. Liu H, Wang ZH, Xin HW, Liu J, Wang QQ, Pang B, et al. Polysaccharide nanocrystals-based chiral nematic structures: from self-assembly mechanisms, regulation, to applications. ACS Nano. 2024;18(34):22675–708. https://doi.org/10.1021/acsnano.4c03130.
9. Zhang H, Johnson AM, Hua Q, Wu J, Liang Y, Karaaslan MA, et al. Size-controlled synthesis of xylan micro/nanoparticles by self-assembly of alkali-extracted xylan. Carbohydr Polym. 2023;315:120944. https://doi.org/10.1016/j.carbpol.2023.120944.
10. Hao X, Lv Z, Wang H, Rao J, Liu Q, Lü B, et al. Top-down production of sustainable and scalable hemicellulose nanocrystals. Biomacromol. 2022;23(11):4607–16. https://doi.org/10.1021/acs.biomac.2c00841.
11. Liu G, Shi K, Sun H. Research progress in hemicellulose-based nanocomposite film as food packaging. Polymers. 2023;15(4):979. https://doi.org/10.3390/polym15040979.
12. Kapil S, Mankoo RK, Dudeja I, Singh A, Kaur J. Structural, antioxidant, antibacterial and biodegradation properties of rice straw xylan (native and modified) based biofilms. Int J Food Sci Technol. 2023;58(5):2772–81. https://doi.org/10.1111/ijfs.16118.
13. Wang S, Xiang Z. Highly stable pickering emulsions with xylan hydrate nanocrystals. Nanomaterials. 2021;11(10):2558. https://doi.org/10.3390/nano11102558.
14. Liu X, Chang M, Zhang H, Ren J. Reinforcement effects of inorganic nanoparticles for PAM-g-carboxymethyl xylan nanocomposite hydrogels. Macromol Mater Eng. 2022;307(10):2200251. https://doi.org/10.1002/mame.202200251.
15. Gao Y, Lipton AS, Wittmer Y, Murray DT, Mortimer JC. A grass-specific cellulose–xylan interaction dominates in sorghum secondary cell walls. Nat Commun. 2020;11(1):6081. https://doi.org/10.1038/s41467-020-19837-z.
16. Herburger K, Franková L, Pičmanová M, Loh JW, Valenzuela-Ortega M, Meulewaeter F, et al. Hetero-trans-β-glucanase produces cellulose-xyloglucan covalent bonds in the cell walls of structural plant tissues and is stimulated by expansin. Mol Plant. 2020;13(7):1047–62.
17. Guo Y, Gao Y, Chen F, Luo J, Qiao M, Li M, et al. Down-regulation of xylan biosynthetic *GhGT47Bs* in cotton impedes fibre elongation and secondary wall thickening during fibre transition. Plant Biotechnol J. 2024;22(2):281–3. https://doi.org/10.1111/pbi.14205.
18. Curry TM, Peña MJ, Urbanowicz BR. An update on xylan structure, biosynthesis, and potential commercial applications. Cell Surf. 2023;9:100101. https://doi.org/10.1016/j.tcsw.2023.100101.
19. Wang H, Yang H, Wen Z, Gao C, Gao Y, Tian Y, et al. Xylan-based nanocompartments orchestrate plant vessel wall patterning. Nat Plants. 2022;8(3):295–306. https://doi.org/10.1038/s41477-022-01113-1.
20. Heinonen E, Henriksson G, Lindström ME, Vilaplana F, Wohlert J. Xylan adsorption on cellulose: preferred alignment and local surface immobilizing effect. Carbohydr Polym. 2022;285:119221. https://doi.org/10.1016/j.carbpol.2022.119221.
21. Pauly M, Gille S, Liu L, Mansoori N, de Souza A, Schultink A, et al. Hemicellulose biosynthesis. Planta. 2013;238(4):627–42. https://doi.org/10.1007/s00425-013-1921-1.
22. Scheller HV, Ulvskov P. Hemicelluloses. Annu Rev Plant Biol. 2010;61:263–89. https://doi.org/10.1146/annurev-arplant-042809-112315.
23. Ragauskas AJ, Williams CK, Davison BH, Britovsek G, Cairney J, Eckert CA, et al. The path forward for biofuels and biomaterials. Science. 2006;311(5760):484–9. https://doi.org/10.1126/science.1114736.
24. Qaseem MF, Shaheen H, Wu A-M. Cell wall hemicellulose for sustainable industrial utilization. Renew Sustain Energy Rev. 2021;144:110996. https://doi.org/10.1016/j.rser.2021.110996.
25. Rennie EA, Scheller HV. Xylan biosynthesis. Curr Opin Biotechnol. 2014;26:100–7. https://doi.org/10.1016/j.copbio.2013.11.013.
26. Teleman A, Tenkanen M, Jacobs A, Dahlman O. Characterization of *O*-acetyl-(4-*O*-methylglucurono)xylan isolated from birch and beech. Carbohydr Res. 2002;337(4):373–7. https://doi.org/10.1016/S0008-6215(01)00327-5.
27. Zhang L, Gao C, Mentink-Vigier F, Tang L, Zhang D, Wang S, et al. Arabinosyl deacetylase modulates the arabinoxylan acetylation profile and secondary wall formation. Plant Cell. 2019;31(5):1113–26. https://doi.org/10.1105/tpc.18.00894.
28. Qaseem MF, Wu A-M. Balanced xylan acetylation is the key regulator of plant growth and development, and cell wall structure and for industrial utilization. Int J Mol Sci. 2020;21(21):2875. https://doi.org/10.3390/ijms21217875.
29. Lü B, Gao Q, Li P, Rao J, Lv Z, Shi M, et al. Natural ultralong hemicelluloses phosphorescence. Cell Rep Phys Sci. 2022;3(9):101015. https://doi.org/10.1016/j.xcrp.2022.101015.
30. Lv Z, Rao J, Lü B, Chen G, Hao X, Guan Y, et al. Microencapsulated phase change material via Pickering emulsion based on xylan nanocrystal for thermoregulating application. Carbohydr Polym. 2023;302:120407. https://doi.org/10.1016/j.carbpol.2022.120407.
31. Wang S, Song T, Qi H, Xiang Z. Exceeding high concentration limits of aqueous dispersion of carbon nanotubes assisted by nanoscale xylan hydrate crystals. Chem Eng J. 2021;419:129602. https://doi.org/10.1016/j.cej.2021.129602.
32. Xiang Z, Jin X, Huang C, Li L, Wu W, Qi H, et al. Water cast film formability of sugarcane bagasse xylans favored by side groups. Cellulose. 2020;27(13):7307–20. https://doi.org/10.1007/s10570-020-03291-7.
33. Hu Z, Wang C, Xiang Z, Lu F. Amino-functionalized glucuronoxylan as an efficient bio-based emulsifier. Cellulose. 2021;28(6):3677–89. https://doi.org/10.1007/s10570-021-03762-5.
34. Wang Y, Zhu Y, Li M, Ji B, Liu S, Liu W, et al. Distinct morphology and self-assembly behavior of xylan nanoparticles are correlated with arabinose side-chains in Sorghum. Carbohydr Polym. 2025;366:123874. https://doi.org/10.1016/j.carbpol.2025.123874.

35. Qaseem MF, Zhang W, Dupree P, Wu A-M. Xylan structural diversity, biosynthesis, and functional regulation in plants. Int J Biol Macromol. 2025;291:138866. https://doi.org/10.1016/j.ijbiomac.2024.138866.
36. Bromley JR, Busse-Wicher M, Tryfona T, Mortimer JC, Zhang Z, Brown DM, et al. GUX1 and GUX2 glucuronyltransferases decorate distinct domains of glucuronoxylan with different substitution patterns. Plant J. 2013;74(3):423–34. https://doi.org/10.1111/tpj.12135.
37. Lee C, Teng Q, Zhong R, Ye Z-H. *Arabidopsis* GUX proteins are glucuronyltransferases responsible for the addition of glucuronic acid side chains onto xylan. Plant Cell Physiol. 2012;53(7):1204–16. https://doi.org/10.1093/pcp/pcs064.
38. Rennie EA, Hansen SF, Baidoo EEK, Hadi MZ, Keasling JD, Scheller HV. Three members of the *Arabidopsis* glycosyltransferase family 8 are xylan glucuronosyltransferases. Plant Physiol. 2012;159(4):1408–17. https://doi.org/10.1104/pp.112.200964.
39. Mortimer JC, Miles GP, Brown DM, Zhang Z, Segura MP, Weimar T, et al. Absence of branches from xylan in *Arabidopsis gux* mutants reveals potential for simplification of lignocellulosic biomass. Proc Natl Acad Sci U S A. 2010;107(40):17409–14. https://doi.org/10.1073/pnas.1005456107.
40. Lee C, Teng Q, Zhong R, Yuan Y, Haghighat M, Ye Z-H. Three *Arabidopsis DUF579* domain-containing GXM proteins are methyltransferases catalyzing 4-*O*-methylation of glucuronic acid on xylan. Plant Cell Physiol. 2012;53(11):1934–49. https://doi.org/10.1093/pcp/pcs138.
41. Ye Z-H, Zhong R. Outstanding questions on xylan biosynthesis. Plant Sci. 2022;325:111476. https://doi.org/10.1016/j.plantsci.2022.111476.
42. Zhong R, Lee C, Cui D, Phillips DR, Adams ER, Jeong H-Y, et al. Identification of xylan arabinosyl 2-*O*-xylosyltransferases catalyzing the addition of 2-*O*-xylosyl residue onto arabinosyl side chains of xylan in grass species. Plant J. 2022;112(1):193–206. https://doi.org/10.1111/tpj.15939.
43. Zhong R, Cui D, Phillips DR, Sims NT, Ye Z-H. Functional analysis of GT61 glycosyltransferases from grass species in xylan substitutions. Planta. 2021;254(6):131. https://doi.org/10.1007/s00425-021-03794-y.
44. Anders N, Wilkinson MD, Lovegrove A, Freeman J, Tryfona T, Pellny TK, et al. Glycosyl transferases in family 61 mediate arabinofuranosyl transfer onto xylan in grasses. Proc Natl Acad Sci USA. 2012;109(3):989–93. https://doi.org/10.1073/pnas.1115858109.
45. Zhong R, Cui D, Phillips DR, Ye Z-H. A novel rice xylosyltransferase catalyzes the addition of 2-*O*-Xylosyl side chains onto the xylan backbone. Plant Cell Physiol. 2018;59(3):554–65. https://doi.org/10.1093/pcp/pcy003.
46. Schultink A, Cheng K, Park YB, Cosgrove DJ, Pauly M. The identification of two arabinosyltransferases from tomato reveals functional equivalency of xyloglucan side chain substituents. Plant Physiol. 2013;163(1):86–94. https://doi.org/10.1104/pp.113.221788.
47. Feijao C, Morreel K, Anders N, Tryfona T, Busse-Wicher M, Kotake T, et al. Hydroxycinnamic acid-modified xylan side chains and their cross-linking products in rice cell walls are reduced in the Xylosyl arabinosyl substitution of xylan 1 mutant. Plant J. 2022;109(5):1152–67. https://doi.org/10.1111/tpj.15620.
48. Zhang X, Henriques R, Lin S-S, Niu Q-W, Chua N-H. Agrobacterium-mediated transformation of *Arabidopsis thaliana* using the floral dip method. Nat Protoc. 2006;1(2):641–6. https://doi.org/10.1038/nprot.2006.97.
49. Wang H, Li S, Wu L, Zou W, Zhang M, Wang Y, et al. Semi-overexpressed *OsMYB86L2* specifically enhances cellulose biosynthesis to maximize bioethanol productivity by cascading lignocellulose depolymerization via integrated rapid-physical and recyclable-chemical processes. Green Chem. 2025. https://doi.org/10.1039/D5GC00658A.
50. Brown DM, Goubet F, Wong VW, Goodacre R, Stephens E, Dupree P, et al. Comparison of five xylan synthesis mutants reveals new insight into the mechanisms of xylan synthesis. Plant J. 2007;52(6):1154–68. https://doi.org/10.1111/j.1365-313X.2007.03307.x.
51. Chiniquy D, Sharma V, Schultink A, Baidoo EE, Rautengarten C, Cheng K, et al. XAX1 from glycosyltransferase family 61 mediates xylosyltransfer to rice xylan. Proc Natl Acad Sci U S A. 2012;109(42):17117–22. https://doi.org/10.1073/pnas.1202079109.
52. Xu N, Zhang W, Ren S, Liu F, Zhao C, Liao H, et al. Hemicelluloses negatively affect lignocellulose crystallinity for high biomass digestibility under NaOH and H_2SO_4 pretreatments in *Miscanthus*. Biotechnol Biofuels. 2012;5(1):58. https://doi.org/10.1186/1754-6834-5-58.
53. Zhang H, Wang Y, Peng H, He B, Li Y, Wang H, et al. Distinct lignocelluloses of plant evolution are optimally selective for complete biomass saccharification and upgrading Cd^{2+}/Pb^{2+} and dye adsorption via desired biosorbent assembly. Bioresour Technol. 2025;417:131856. https://doi.org/10.1016/j.biortech.2024.131856.
54. Peng H, Zhao W, Liu J, Liu P, Yu H, Deng J, et al. Distinct cellulose nanofibrils generated for improved Pickering emulsions and lignocellulose-degradation enzyme secretion coupled with high bioethanol production in natural rice mutants. Green Chem. 2022;24(7):2975–87. https://doi.org/10.1039/D1GC04447H.
55. Alam A, Zhang R, Liu P, Huang J, Wang Y, Hu Z, et al. A finalized determinant for complete lignocellulose enzymatic saccharification potential to maximize bioethanol production in bioenergy *Miscanthus*. Biotechnol Biofuels. 2019;12(1):99. https://doi.org/10.1186/s13068-019-1437-4.
56. Meng Z, Sawada D, Laine C, Ogawa Y, Virtanen T, Nishiyama Y, et al. Bottom-up construction of xylan nanocrystals in dimethyl sulfoxide. Biomacromol. 2021;22(2):898–906. https://doi.org/10.1021/acs.biomac.0c01600.
57. Li Q, Xie B, Wang Y, Wang Y, Peng L, Li Y, et al. Cellulose nanofibrils from *Miscanthus* floridulus straw as green particle emulsifier for O/W Pickering emulsion. Food Hydrocolloids. 2019;97:105214. https://doi.org/10.1016/j.foodhyd.2019.105214.
58. Yu H, Zhang G, Liu J, Liu P, Peng H, Teng Z, et al. A functional cascading of lignin modification via repression of caffeic acid *O*-methyltransferase for bioproduction and anti-oxidation in rice. J Adv Res. 2025. https://doi.org/10.1016/j.jare.2025.01.048.
59. Li T, Peng H, He B, Hu C, Zhang H, Li Y, et al. Cellulose de-polymerization is selective for bioethanol refinery and multi-functional biochar assembly using brittle stalk of corn mutant. Int J Biol Macromol. 2024;264:130448. https://doi.org/10.1016/j.ijbiomac.2024.130448.
60. Huang Q, Hu D, Chen M, Bao C, Jin X. Sequential removal of aniline and heavy metal ions by jute fiber biosorbents: a practical design of modifying adsorbent with reactive adsorbate. J Mol Liq. 2019;285:288–98. https://doi.org/10.1016/j.molliq.2019.04.115.
61. Fan C, Feng S, Huang J, Wang Y, Wu L, Li X, et al. *AtCesA8*-driven *OsSUS3* expression leads to largely enhanced biomass saccharification and lodging resistance by distinctively altering lignocellulose features in rice. Biotechnol Biofuels. 2017;10(1):221. https://doi.org/10.1186/s13068-017-0911-0.
62. Ai Y, Wang H, Liu P, Yu H, Sun M, Zhang R, et al. Insights into contrastive cellulose nanofibrils assembly and nanocrystals catalysis from dual regulations of plant cell walls. Sci Bull. 2024;69(24):3815–9. https://doi.org/10.1016/j.scib.2024.06.013.
63. Zhang X, Wei Y, Chen M, Xiao N, Zhang J, Liu C. Development of functional chitosan-based composite films incorporated with hemicelluloses: effect on physicochemical properties. Carbohydr Polym. 2020;246:116489. https://doi.org/10.1016/j.carbpol.2020.116489.
64. Zhang X, Xiao N, Chen M, Wei Y, Liu C. Functional packaging films originating from hemicelluloses laurate by direct transesterification in ionic liquid. Carbohydr Polym. 2020;229:115336. https://doi.org/10.1016/j.carbpol.2019.115336.
65. Guan Y, Qi X-M, Chen G-G, Peng F, Sun R-C. Facile approach to prepare drug-loading film from hemicelluloses and chitosan. Carbohydr Polym. 2016;153:542–8. https://doi.org/10.1016/j.carbpol.2016.08.008.
66. Wang Y, Lu C, Cao X, Wang Q, Yang G, Chen J. Porous carbon spheres derived from hemicelluloses for supercapacitor application. Int J Mol Sci. 2022;23(13):7101. https://doi.org/10.3390/ijms23137101.
67. Mikkonen KS, Xu C, Berton-Carabin C, Schroën K. Spruce galactoglucomannans in rapeseed oil-in-water emulsions: efficient stabilization performance and structural partitioning. Food Hydrocolloid. 2016;52:615–24. https://doi.org/10.1016/j.foodhyd.2015.08.009.
68. Wang L, Wu M, Liu H-M. Emulsifying and physicochemical properties of soy hull hemicelluloses-soy protein isolate conjugates. Carbohydr Polym. 2017;163:181–90. https://doi.org/10.1016/j.carbpol.2017.01.069.
69. Li Y-F, Yue P-P, Hao X, Bian J, Ren J-L, Peng F, et al. Comparison of emulsifying capacity of two hemicelluloses from moso bamboo in soy oil-in-water emulsions. RSC Adv. 2020;10(8):4657–63. https://doi.org/10.1039/C9RA08636F.
70. Yong Q, Xu J, Wang L, Tirri T, Gao H, Liao Y, et al. Synthesis of galactoglucomannan-based latex via emulsion polymerization. Carbohydr Polym. 2022;291:119565. https://doi.org/10.1016/j.carbpol.2022.119565.
71 Syafri E, Jamaluddin, Sari NH, Mahardika M, Amanda P, Ilyas RA. Isolation and characterization of cellulose nanofibers from Agave gigantea by

chemical-mechanical treatment. Int J Biol Macromol. 2022;200:25–33. https://doi.org/10.1016/j.ijbiomac.2021.12.111.
72. Li F, Zhang M, Guo K, Hu Z, Zhang R, Feng Y, et al. High-level hemicellulosic arabinose predominately affects lignocellulose crystallinity for genetically enhancing both plant lodging resistance and biomass enzymatic digestibility in rice mutants. Plant Biotechnol J. 2015;13(4):514–25. https://doi.org/10.1111/pbi.12276.

Publisher's Note